

Die filling optimization using three-dimensional discrete element modeling

C. Bierwisch^a T. Kraft^a H. Riedel^a M. Moseler^a

^a*Fraunhofer-Institut für Werkstoffmechanik IWM, Wöhlerstraße 11, 79108
Freiburg, Germany*

Abstract

Inhomogeneous density distributions after die filling are a ubiquitous problem in powder technological part production. In this paper, numerical simulations of the die filling process in realistic, three-dimensional (3D) cavities are presented using the discrete element method with both multi-sphere and single sphere grain models. Good agreement was found between calculated and experimentally measured density distributions. The formation of an inhomogeneous distribution is discussed by a time-resolved analysis of the filling process. Grain rearrangement and densification during subsequent feeding shoe passages are characterized. The shoe velocity was tested for its influence on the density homogeneity. Suggestions for density homogenization with the application of cavity oscillations or volumetric filling are given. A density homogeneity index is introduced. The application of a coarse graining scheme circumvents the intrinsic difficulty of non-manageable grain numbers in 3D filling simulations. The validity and limitations of this scheme are discussed.

Key words: Die filling, Density distribution, Density homogeneity index, Discrete element method, Coarse graining

1 Introduction

Powder compaction and sintering [1] are important techniques for the mass production of geometrically complex parts. The standard processing route [2,3] starts with the die filling step. Powder is poured from a reservoir into the feeding shoe, which then passes the cavity one or more times thereby delivering powder into it. The next step is uniaxial compaction of the powder creating a relatively brittle green body. Finally, the green body is ejected from the cavity and sintered in a furnace where thermal activation below the melting point produces a fully dense structure [1]. Necks form and grow between adjacent grains thereby eliminating the porosity of the part.

Generally, the filling of the die and the subsequent compaction lead to inhomogeneous distributions of the powder in the green body [4,5]. Green density gradients yield inhomogeneous shrinkage during sintering and therefore distortions of the sintered part. Thus, it is desirable to identify mechanisms leading to density inhomogeneities during the die filling step. This knowledge can then be used to improve the overall filling homogeneity by appropriate process parameter adjustment. The objectives of fill density prediction and homogenization establish the motivation for the present study. In this regard a numerical approach is beneficial in two ways. First, density information is accessible at any spatial or temporal resolution. Second, variations of process parameters can be tested and analyzed with comparably little effort. In addition, calculated densities can directly be used as an initial condition for compaction and

Email addresses: claas.bierwisch@iwm.fraunhofer.de (C. Bierwisch),
michael.moseler@iwm.fraunhofer.de (M. Moseler).
URL: www.iwm.fraunhofer.de (M. Moseler).

sintering simulations in order to model the complete processing route [6].

Only few simulations of die filling can be found in the literature. Wu *et al.* [7,8] and Guo *et al.* [9,10] were the first to use the discrete element method (DEM) [11] for die filling simulations in order to investigate the influence of escaping air and cavity geometry. Riera *et al.* [12] modeled die filling using a scheme based on the finite element method. Gustafsson *et al.* [13] developed a smoothed particle hydrodynamics model for the same purpose. Common to these approaches is that they are restricted to two dimensions and, therefore, provide at most a generic understanding of the filling process. No studies incorporating a 3D description are known to the authors except for their recent publication [14].

In the present work 3D DEM simulations are used to predict and optimize density distributions in die filling. The individual model grains are either composed of several primary spheres to mimic the irregularity of commonly used industrial powders or represented by simple spheres. Parameters controlling friction and cohesion of the DEM model are adjusted to reproduce the filling behavior of iron based Distaloy AE powder. For validation, simulated density distributions in different cavities are compared with experimentally measured data by Burch *et al.* [4]. Access to trajectories of every grain within the simulations render two new ways of die filling assessment possible: First, the formation of an inhomogeneous density distribution is investigated using a time-resolved analysis of the filling stage for the narrow ring cavity. Second, the effect of subsequent shoe passages on grain displacement and surface densification is studied by means of displacement fields. A variety of process parameters are tested numerically for their influence on the final density distribution: Variations of the feeding shoe velocity are carried out. Linear os-

cillations are applied to either shoe or cavity during the filling process. Linear and rotational oscillations with different frequencies are applied to the cavity after the shoe passage. By using a moveable lower punch volumetric filling is investigated as an alternative die filling method.

An intrinsic difficulty of die filling simulations in 3D is the large number of grains involved. This challenge is resolved by using larger model grains. The application of certain scaling rules for the intergranular forces ensures that dynamic and static properties of the granular material are independent of the actual grain size except for boundary effects [14].

This article is organized as follows. The numerical method is explained in Sec. 2. A summary of the used model parameters, the adjustment procedure, and the coarse graining method are presented in Sec. 3. Section 4 contains the main results of the study. The discussion is given in Sec. 5. The article ends with a general conclusion in Sec. 6.

2 Simulation method

DEM calculations are used for all simulations in the present study. Pioneering work on the description of powders and grains using this approach was done by Cundall [11], Campbell [15], Walton [16], Haff [17], and Herrmann [18]. DEM is currently developing into a versatile simulation method for particulate materials such as rocks, sand, and powders [19]. The dynamic behavior of an ensemble of grains is governed by Newton's equations of motion,

$$m_k \dot{\mathbf{v}}_k = \mathbf{f}_k, \quad \dot{\mathbf{r}}_k = \mathbf{v}_k, \tag{1}$$

$$\underline{I}_k \dot{\boldsymbol{\omega}}_k = \mathbf{t}_k, \tag{2}$$

where m_k is the mass, \mathbf{r}_k is the center of mass position, \mathbf{v}_k is the velocity, I_k is the inertia tensor, and $\boldsymbol{\omega}_k$ is the angular velocity of the grain with label k . The total force acting on the grain is \mathbf{f}_k while the total torque is \mathbf{t}_k . The grains interact via explicitly defined force laws and they can be affected by external forces such as gravity. Equations (1) and (2) are solved by explicit time integration using a velocity Verlet scheme [20] with fixed timestep Δt ,

$$\mathbf{r}_k(t + \Delta t) = \mathbf{r}_k(t) + \mathbf{v}_k(t)\Delta t + \frac{\mathbf{f}_k(t)\Delta t^2}{2m_k}, \quad (3)$$

$$\mathbf{v}_k(t + \Delta t) = \mathbf{v}_k(t) + \frac{(\mathbf{f}_k(t) + \mathbf{f}_k(t + \Delta t)) \Delta t}{2m_k}, \quad (4)$$

$$\boldsymbol{\omega}_k(t + \Delta t) = \boldsymbol{\omega}_k(t) + \frac{I_k^{-1} (\mathbf{t}_k(t) + \mathbf{t}_k(t + \Delta t)) \Delta t}{2}. \quad (5)$$

Figure 1 shows DEM model grains and a picture of a typical iron powder grain. The brand name of the powder is Distaloy AE. A former study revealed that mimicking the shape of irregular grains—in contrast to simple spheres—is necessary in order to reproduce both static (e.g. angle of repose) and dynamic (e.g. flow rates) properties [14]. The influence of the grain shape on flow rates was also stressed in previous numerical investigations on die filling in two dimensions [8,21]. In this work two DEM grain models were used. Mainly, a multi-sphere model was employed where a grain is composed of primary spheres which form the elementary objects. A similar approach using non-spherical grain shapes was first introduced to model granular heaps in two dimensions [22]. The primary spheres are rigidly connected, i.e. the grains have no vibrational degrees of freedom and cannot fracture. Although the morphology of the Distaloy AE grains is not covered in detail the model allows for inclusion of geometrical interlocking of different grains.

When two primary spheres of different grains come into contact, i.e. their sur-

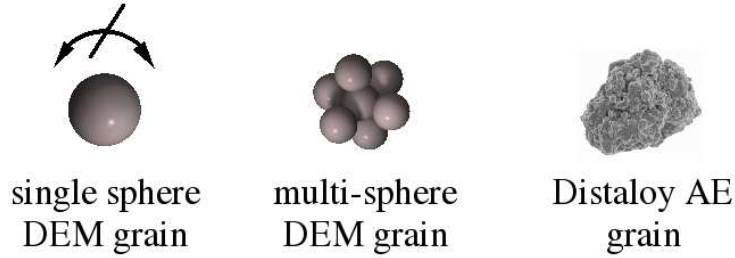


Fig. 1. DEM grains as used in the simulations and image of a real Distaloy AE grain.

faces touch, the forces acting on the spheres are calculated. The total force and torque acting on a grain is then given by summation over its primary spheres. The equations of motion are solved under the constraint of the stiffness of each grain. For this purpose a rigid body motion solver is used, which is based on a quaternion representation of the Euler angles of rotation [23]. The components of the inertia tensors \underline{I}_k of the grains are obtained via summation over the constituent primary spheres,

$$\left(\underline{I}_k\right)^{\alpha\beta} = \sum_i \left(\frac{2}{5} m_i R_i^2 \delta^{\alpha\beta} + m_i \left(\mathbf{b}_i^2 \delta^{\alpha\beta} - b_i^\alpha b_i^\beta \right) \right), \quad (6)$$

where a sphere with label i has mass m_i , radius R_i , and is located at $\mathbf{b}_i = (b_i^x, b_i^y, b_i^z)$ with respect to the center of mass of the composed grain. $\alpha, \beta \in (x, y, z)$ and $\delta^{\alpha\beta}$ is the Kronecker delta.

For comparison, simple spheres without rotational degrees of freedom were assessed as a second DEM grain model. It was found that its performance in describing a real powder comprehensively is inferior to the multi-sphere model while it is superior to a single sphere model with rotational degrees of freedom [14]. Of course, a single sphere model is computationally more efficient than a multi-sphere model.

2.1 Force Laws

The primary spheres labeled i and j are described by the position vectors $\mathbf{r}_{i,j}$, the velocities $\mathbf{v}_{i,j}$, and the radii $R_{i,j}$. During contact they undergo the deformation $h_{ij} = R_i + R_j - |\mathbf{r}_{ij}|$, $\mathbf{r}_{ij} = \mathbf{r}_i - \mathbf{r}_j$. No forces are applied if $h_{ij} < 0$.

Along the unit vector normal to the contact plane, $\hat{\mathbf{r}}_{ij} = \mathbf{r}_{ij}/|\mathbf{r}_{ij}|$, act three forces: Elastic repulsion, cohesion, and viscous damping. Repulsion is taken to be of Hertzian type [24],

$$\mathbf{f}_{ij}^e = \left(\frac{2}{3} \tilde{E} \sqrt{R_{\text{eff}}} h_{ij}^{3/2} \right) \hat{\mathbf{r}}_{ij}. \quad (7)$$

$\tilde{E} = E/(1 - \nu^2)$, where E the Young's modulus, ν is Poisson's ratio, and $R_{\text{eff}} = R_i R_j / (R_i + R_j)$ is an effective radius. Cohesion is considered using the Johnson-Kendall-Roberts model [25],

$$\mathbf{f}_{ij}^{\text{coh}} = - \left(\sqrt{4\pi w \tilde{E}} R_{\text{eff}}^{3/4} h_{ij}^{3/4} \right) \hat{\mathbf{r}}_{ij}, \quad (8)$$

which is the natural extension of the Hertzian contact law upon introducing the free surface energy per unit area, $w/2$. Energy dissipation during the contact is described by a viscous force [26],

$$\mathbf{f}_{ij}^v = - \left(\gamma_n \sqrt{R_{\text{eff}}} h_{ij} \right) (\mathbf{v}_i - \mathbf{v}_j) \cdot \hat{\mathbf{r}}_{ij} \hat{\mathbf{r}}_{ij}, \quad (9)$$

where γ_n is an empirical damping parameter.

Static and sliding friction is modeled in the sense of Cundall and Strack [11].

An imaginary spring is applied at the initial contact points of the two primary spheres. The elongation $\boldsymbol{\xi}_{ij}$ of the spring is tracked during contact evolution.

A restoring force acts at each contact point directing along the spring. This force is Coulomb-like, because its magnitude is limited by the product of the

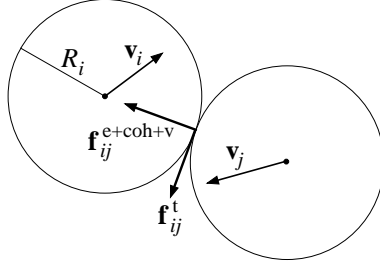


Fig. 2. Contact forces between two primary spheres.

current normal force at the contact and a friction coefficient μ ,

$$\mathbf{f}_{ij}^t = -\min \left[\kappa_t \sqrt{\frac{h_{ij}}{R_{\text{eff}}}} |\boldsymbol{\xi}_{ij}|, \mu |\mathbf{f}_{ij}^e + \mathbf{f}_{ij}^v| \right] \boldsymbol{\xi}_{ij} / |\boldsymbol{\xi}_{ij}|, \quad (10)$$

where κ_t is the spring constant. Fig. 2 gives an overview of the forces acting in a binary collision.

In addition to the contact forces, gravitational acceleration g in z -direction (unit vector $\hat{\mathbf{z}}$),

$$\mathbf{f}_i^{\text{grav}} = -m_i g \hat{\mathbf{z}}, \quad (11)$$

and Stokes' drag due to air viscosity μ_a ,

$$\mathbf{f}_i^{\text{stokes}} = -6\pi\mu_a R_i \mathbf{v}_i. \quad (12)$$

are taken into account. Note that for typical grain velocities in die filling (i.e. up to 1 m/s) the influence of Stokes' drag is extremely small compared to all other forces.

2.2 Cavity, feeding shoe, and initial setup

The walls of cavity and feeding shoe are modeled by overlapping spheres with radius R_w . The typical distance between the centers of two adjacent wall spheres is $1.6R_w$. The force laws for wall-grain interaction are the same as for

grain-grain interaction. Friction and cohesion at the wall is different compared to bulk behavior of the powder. Therefore, instead of μ and w a wall friction coefficient, μ_w , and a surface energy, w_w , are used in Eqs. (8) and (10) for wall-grain interaction. It was checked that variations of R_w , wall sphere distance, and μ_w have only minor influences the presented cavity filling properties. The mass of wall spheres is set to be infinite. The movement of the feeding shoe is externally defined by displacement of all associated spheres. The same applies for the case of shoe or cavity oscillations.

The initial distribution of the grains in the feeding shoe mimics powder transfer from a hose. The grains are positioned above the feeding shoe on a lattice with some random offset and random angular velocities but without overlap. Then the grains are allowed to settle under gravity. Shoe movement starts after the grains come to rest in a random packing.

2.3 Density calculation

Three-dimensional Voronoi tessellation is used for the calculation of density distributions. The set of all points in space which are closer to a certain grain than to any other forms the Voronoi cell of that grain (see Fig. 3 for details). The diameter of the grains, i.e. the longest distance between surface points of the primary spheres, is denoted as d . The Voronoi cell volume is calculated by means of numerical integration. Therefore, the complete simulation space is discretized using a cartesian grid with a box edge length smaller than $0.1d$. Each box is then assigned to the nearest grain. The sum of the volumes of all boxes assigned to a certain grain is a good approximation of the Voronoi cell volume, $V_{\text{cell},k}$, of the grain. The fraction of grain volume, V_k , and Voronoi cell

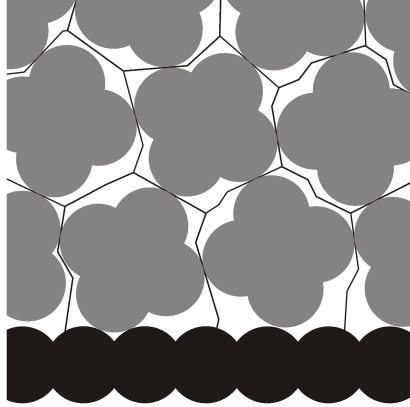


Fig. 3. Two-dimensional schematic of Voronoi space tessellation for density computation. Powder grains are drawn in gray and spheres forming a wall are drawn in black. Straight lines separate the Voronoi cells between grains. Note that the Voronoi cell boundaries between wall spheres and powder grains are defined by the surface of the wall spheres. Adapted from Ref. [14].

volume then defines a local density (volume fraction) at the position of the grain with label k , $\rho_k = V_k/V_{\text{cell},k}$. Continuous density maps are obtained by averaging over grain densities using Gaussian distance weighting with standard deviation σ ,

$$\rho(\mathbf{r}) = \frac{\sum_k \rho_k \exp\left(-\frac{(\mathbf{r}-\mathbf{r}_k)^2}{2\sigma^2}\right)}{\sum_k \exp\left(-\frac{(\mathbf{r}-\mathbf{r}_k)^2}{2\sigma^2}\right)}. \quad (13)$$

For $\sigma/d \leq 1/4$ density variations are resolved at grain level while larger values of σ/d yield smoother maps.

3 Adjustment of model parameters

Burch *et al.* [4] used a narrow ring cavity and a stepped ring cavity (see Fig. 4) for filling experiments with Distaloy AE powder. The feeding shoe moves in the $+x$ -direction during its first passage. The filling height was measured for

the case of incomplete filling using high feeding shoe velocities. Density distributions were evaluated using X-ray computer tomography technique in completely filled cavities. These experiments provide the basis for adjustment of the free model parameters in the present paper and are used to validate the simulations.

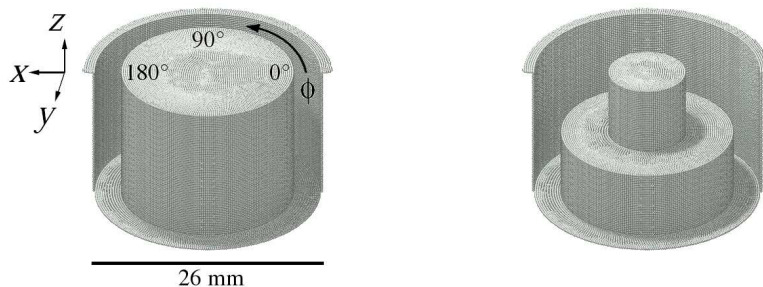


Fig. 4. Models of narrow ring cavity and stepped ring cavity used for filling experiments and simulations. The feeding shoe moves from right to left during its first passage. Adapted from Ref. [14].

A realistic value for the Young's modulus E requires an extremely small timestep yielding long computational times. Therefore, the values for E were chosen significantly lower, i.e. about four orders of magnitude, than in reality. The influence of this reduction was analyzed with the main outcome that the results are not affected substantially as long as $E \geq 10^7$ Pa, which is comparable with the reduction of E in previous studies on granular flow [27].

The dissipative parameter, γ_n , does not affect powder flow properties significantly. For grains settling under gravity, a smaller value of γ_n leads to a denser packing [28]. It was checked that relative variations in density distributions do not depend on the actual choice of γ_n ; only the mean value is shifted. Thus, γ_n has been set to a fixed value throughout the study.

The variation of either κ_t or μ does influence hopper outflow rates within a similar range while the other quantity is kept constant [29]. Therefore, it is reasonable to use just one of these two parameters for adjustment of powder friction. In this case μ was chosen as a free parameter. The tangential spring constant κ_t was given a fixed value.

The model parameters controlling friction, μ , and cohesion, w , were adjusted in an iterative process such that the filling level of the narrow ring cavity after one passage at a shoe velocity of $v_s=0.2$ m/s is reproduced. Figure 5 displays both experimental and simulation results of filling levels plotted as a function of the azimuthal angle. The shoe reaches the $0/360^\circ$ position first and the 180° position last on its passage. Good agreement between experiment and simulation could be achieved. Especially the slopes around 90° and 270° , respectively, are reproduced well. Thereby, the multi-sphere model performs slightly better than the single sphere model. A more detailed study on model parameter adjustment was given in Ref. [14].

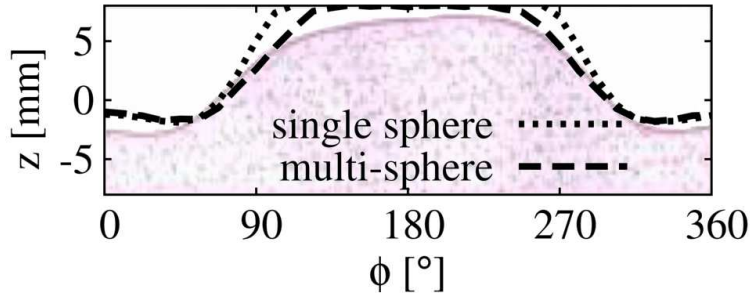


Fig. 5. Filling levels in the narrow ring after one shoe passage with $v_s=0.2$ m/s. Experiment with Distaloy AE (shaded area) and simulations. Adapted from Ref. [14].

The surface energy for wall-grain interaction, w_w , was set to zero. The wall friction coefficient was set to a value of $\mu_w=0.15$ based on experimental measurements [30]. Table 1 gives a summary of all simulation parameters. The

friction coefficient of $\mu=1.0$ for the multi-sphere model may appear relatively high. Yet, simulations using $\mu=0.3$ yield similar results for the filling level. The influence of the friction coefficient on the simulation results was tested for further selected setups. The main outcome is an increase in density for a lowered value of μ . However, observed features of the spatial density distributions remain unaffected by varying the friction coefficient. This might indicate that the effective friction between multi-sphere grains is rather caused by their morphology than by explicit friction modeling via Eq. (10).

Simulations with smaller multi-sphere grains than $d=470\ \mu\text{m}$ could not be carried out for computational reasons. A single simulation using this grain size incorporates roughly 4 million primary spheres, which have to be propagated for about 1 s real time. This takes about 130 hours in a parallel computation using 35 Xeon 2.0 GHz CPUs. Thus, it is not possible to carry out filling simulations of cavities with typical length scales in the range of centimeters, while using grains with mean diameters around $100\ \mu\text{m}$, which are typical for Distaloy AE.

Coarse graining was applied in order to reduce the number of grains involved in the simulations. Numerical tests showed that properties like volume fraction, angle of repose, and flow rates are independent of grain size given that the parameters γ_n , κ_t , and w are scaled in proportion to R , while all other parameters are kept constant [14]. These particular scaling laws are the result of a dimensional analysis. However, boundary effects are not negligible if the grain size becomes comparable to the length scale of cavity features.

It was checked that coarse graining by up to a factor 10 compared to the real grain size does not significantly change the flow and filling characteristics

Table 1

Parameters used in the simulations. For the multi-sphere model the radius R refers to the primary spheres, while the diameter d , volume V , and mass m refer to the composed grains.

Parameter	single sphere	small multi-sphere	large multi-sphere
primary spheres [#]	$1.2 \cdot 10^6$	$3.7 \cdot 10^6$	$4.7 \cdot 10^5$
R [m]	$1.5 \cdot 10^{-4}$	$7.84 \cdot 10^{-5}$	$1.568 \cdot 10^{-4}$
d [m]	$3.0 \cdot 10^{-4}$	$4.7 \cdot 10^{-4}$	$9.4 \cdot 10^{-4}$
V [m ³]	$1.41 \cdot 10^{-11}$	$1.41 \cdot 10^{-11}$	$1.128 \cdot 10^{-10}$
m [kg]	$7.63 \cdot 10^{-8}$	$7.63 \cdot 10^{-8}$	$6.104 \cdot 10^{-7}$
μ []	0.5	1.0	1.0
w/R [J/m ³]	0.0	63.8	63.8
\tilde{E} [Pa]		10^7	
γ_n/R [Pa s/m]		10^6	
κ_t/R [Pa]		10^6	
R_w [m]		$1.5 \cdot 10^{-4}$	
μ_w []		0.15	
w_w [J/m ²]		0.0	
g [m/s ²]		9.81	
μ_a [Pa s]		$2.0 \cdot 10^{-5}$	
Δt [s]		$1.9 \cdot 10^{-6}$	

for the considered cavity dimensions. Figure 6 displays density distributions plotted against azimuthal angle and height using the multi-sphere model with grain diameters $d=470\ \mu\text{m}$, $d=940\ \mu\text{m}$, and $d=1.88\ \text{mm}$, respectively.

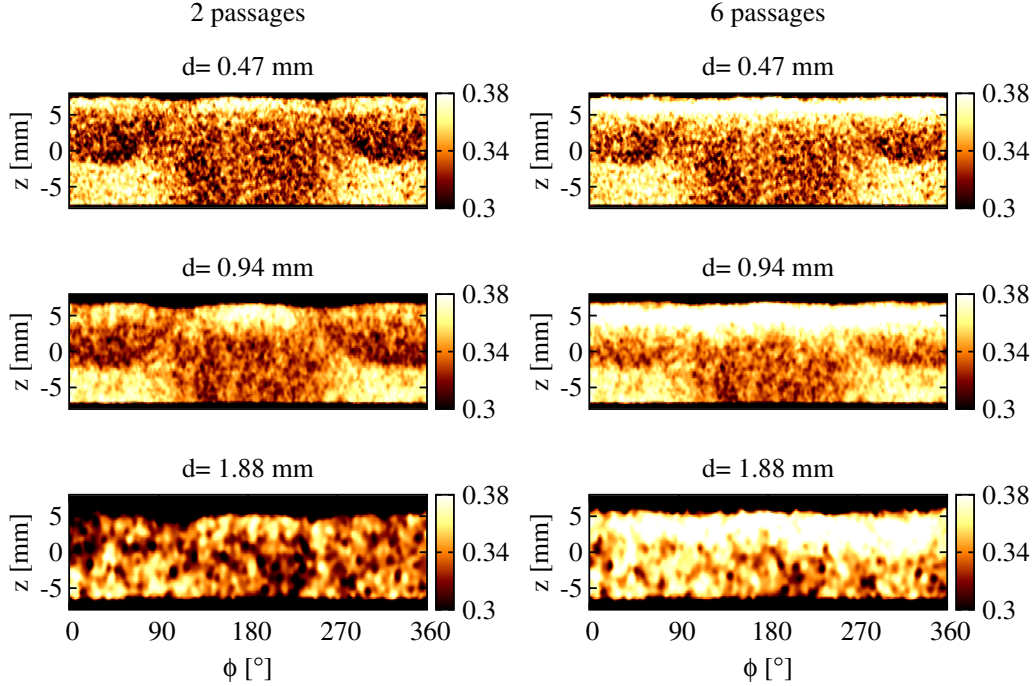


Fig. 6. Influence of coarse graining on simulated density distributions for the narrow ring cavity using $v_s=0.2\ \text{m/s}$ after two and six feeding shoe passages, respectively.

All of the main features of the distributions in the narrow ring cavity appear for $d=470\ \mu\text{m}$ and $d=940\ \mu\text{m}$. Yet, after six shoe passages the densified surface layer reaches deeper into the cavity for $d=940\ \mu\text{m}$. The densification depth is apparently related to the actual grain size which confirms a proposition by Hjortsberg *et al.* [31]. A larger zone of low density can be observed at the bottom of the cavities when using $d=940\ \mu\text{m}$ grains in comparison to $d=470\ \mu\text{m}$. This zone is the boundary layer of grains where the density is reduced due to the confining cavity walls [14,32].

The simulations with $d=1.88$ mm differ strongly from those using smaller grains. Azimuthal density variations are hardly observable while the surface densification after six shoe passages reaches halfway through the die. The boundary layers at the bottom are roughly twice as large compared to $d=940$ μm .

4 Results

4.1 Prediction of density distributions

Figures 8 and 7 show comparisons of measured and calculated density distributions. For the narrow ring cavity the density is plotted against azimuthal angle and height. For the stepped ring cavity the density was evaluated in a diametral vertical slice perpendicular to the direction of shoe movement, i.e. the x -axis. Only for the stepped ring cavity quantitative densities are published in Ref. [4]. Thus, the comparison between experiments and simulations for the narrow ring cavity is of qualitative nature. The simulations in this section were carried out using multi-sphere grains with diameter $d=470$ μm and single sphere grains with $d=300$ μm . The experimental Distaloy AE grains have a mean diameter of about 100 μm .

After a single shoe passage at $v_s=0.09$ m/s significant features in the experimental distribution of the narrow ring are a comparably low density around 180° throughout the whole height (see left panel of Fig. 7). For angles smaller than 90° and larger than 270° the density in the lower half of the ring is markedly higher while surface densification is slightly reduced. All features found in the experiment are reproduced by the simulations. Note that surface

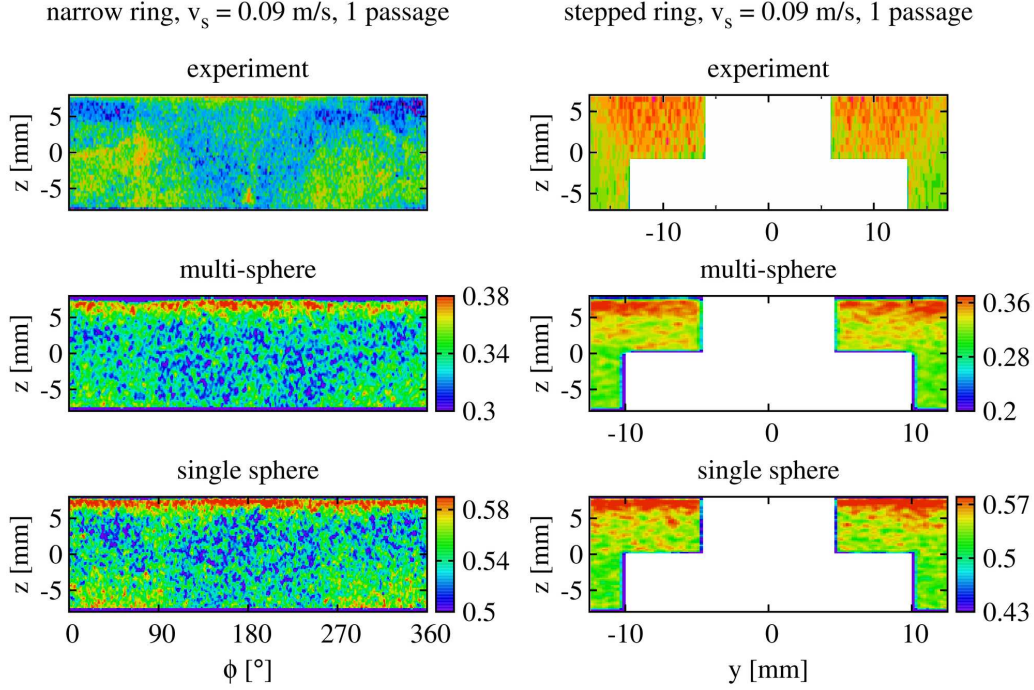


Fig. 7. Comparison of density distributions from experiments [4] and simulations for the narrow ring and stepped ring using shoe velocity $v_s=0.09$ m/s. Compare Fig. 4 for the shoe movement. Color scales refer only to simulations. Adapted from Refs. [4,14].

densification is slightly exaggerated due to coarse graining, as the model grains are three to five times larger than the experimental grains.

The experimental density in the upper part of the stepped ring is significantly higher (109% of mean density [4]) compared to the lower part (92% of mean density) where the cavity is narrower (see right panel of Fig. 7). The simulations resemble the experimental observations. For the multi-sphere model the simulated density near the surface of the stepped ring is about 0.36, while it is about 0.30 in the lower narrow part. Thus, the relative differences compared to the mean density of 0.33 are in very good agreement with the experimental results. The results for the single sphere model are comparable. In this case

the density varies from about 0.51 in the lower part to about 0.58 near the surface.

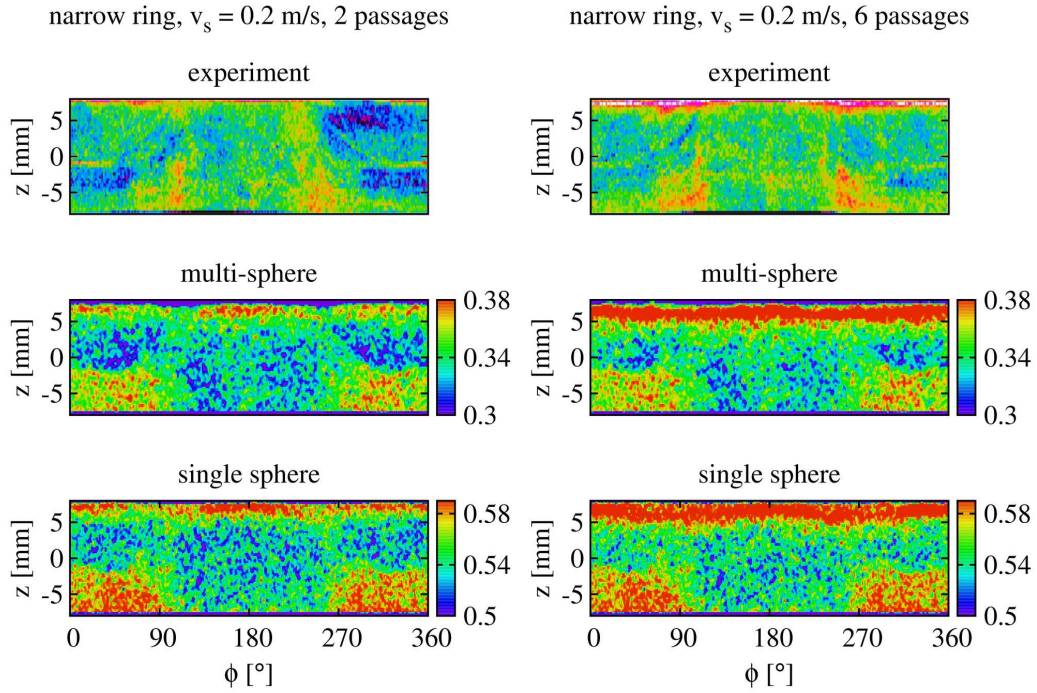


Fig. 8. Same as Fig. 7 but for narrow ring using $v_s=0.2$ m/s and more shoe passages. Adapted from Refs. [4,14].

After two passages at $v_s=0.2$ m/s (see left panel of Fig. 8) the experimental density in the 180° region is higher compared to the case of $v_s=0.09$ m/s and one passage. The highest density is found in small areas at the bottom of the cavity close to 90° and 270° . Around $0^\circ/360^\circ$ the density is lower except for a thin horizontal line at half height, corresponding to the filling level after a single passage. Gaps within the dense surface layer are located around 90° and 270° . The simulations are in agreement with the experiment except for some missing details around $0^\circ/360^\circ$.

After six shoe passages (see right panel of Fig. 8) further densification at the surface and in the region below 90° and above 270° occurs in the experiment.

The region around 180° is only slightly densified. The simulations reproduce the experimental features. However, the depth of surface densification is over-predicted.

All of the simulation results for the multi-sphere grain model are very similar to those for the single sphere model. Apparently, a simple approximation of grain shape and interaction is sufficient in order to describe density features at the presented level of detail. However, due to the bad overall performance of the single sphere model in various flow setups [14] further investigations in this work were carried out using the multi-sphere model.

4.2 Density formation during filling

The case of filling the narrow ring cavity at $v_s=0.09$ m/s was chosen as an example to illustrate the evolution of the density distribution during the filling process. The simulations in this section carried out using multi-sphere grains with diameter $d=470$ μm . Figure 9 depicts density maps, $\rho(\phi, z, t_0 + n\Delta t)$, for intervals of $\Delta t=150$ ms and $t_0=100$ ms. In addition, density difference maps, $\rho(\phi, z, t_0 + n\Delta t) - \rho(\phi, z, t_0 + n\Delta t - 50 \text{ ms})$, are displayed. The density difference plots reveal that density changes due to the newly arriving grains only occur close to the current surface. No significant densification can be observed in the bulk regions below the surface. It was checked that for a lower friction coefficient, $\mu=0.3$, very similar results are obtained.

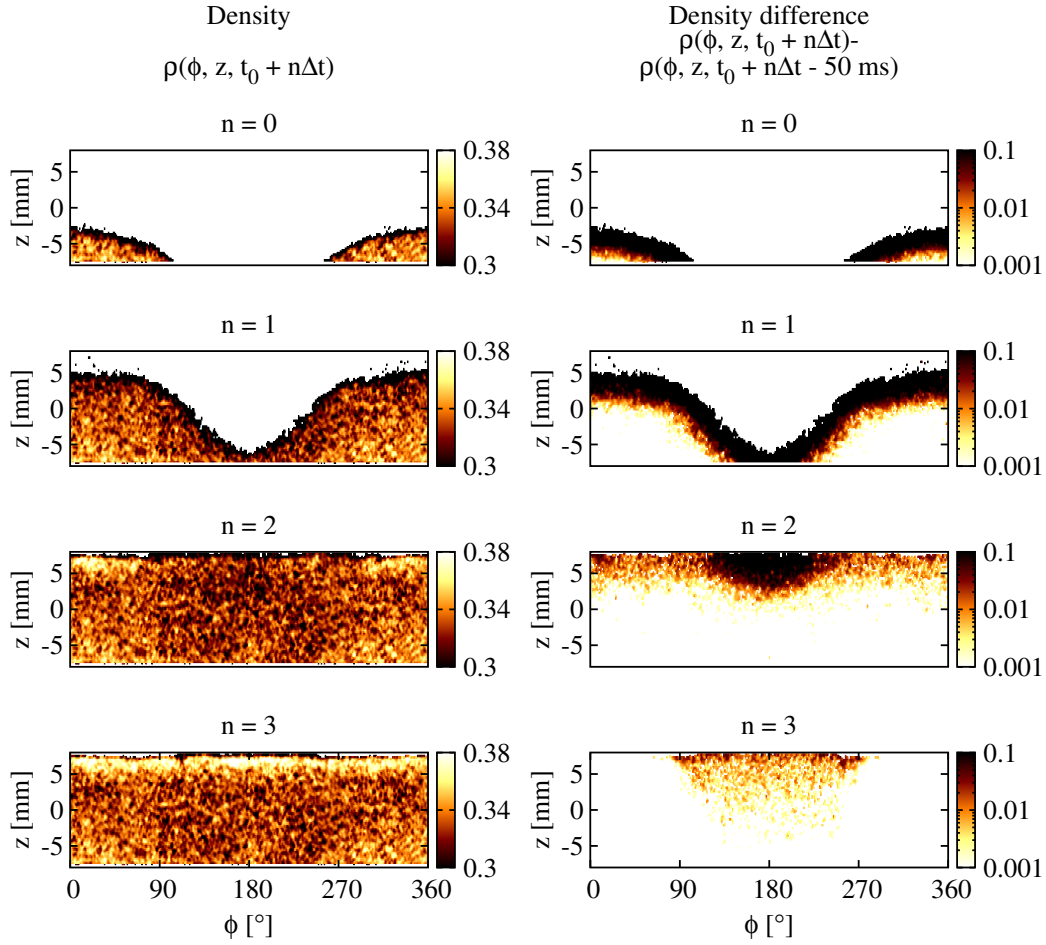


Fig. 9. Density evolution during filling of the narrow ring at $v_s=0.09$ m/s.

4.3 Grain displacement during subsequent shoe passages

Grain displacement fields are shown in Fig. 10 as they occur between subsequent shoe passages at $v_s=0.2$ m/s for the narrow ring and for a wide ring. All simulations presented from now on were carried out using multi-sphere grains with diameter $d=940$ μm . The cavities are completely filled after the second shoe passage. Thus, the displacement fields are displayed from the third passage on. The strongest displacement is found within the topmost grain layers, which are in direct contact with the powder inside the passing shoe. The re-

arrangement is affected by the cavity geometry. Displacements at the surface are especially strong near the 90° and 270° regions for the narrow ring, while they are rather homogeneous around the wide ring. In the narrow ring at 0° and 180° large grain displacements along the direction of shoe movement are apparently suppressed by the cavity walls. In the narrow ring displacements above the chosen limit occur down to approximately one third of the cavity height. For the wide ring the depth of displacement increases along the direction of shoe motion. These observations confirm a mechanism as proposed by Hjortsberg *et al.* [31], who ascribed compaction during subsequent shoe passages to shear induced granular rearrangement. Independent of cavity geometry it is observed that the strength of compaction decreases with the number of passages.

4.4 *Influence of shoe velocity*

For both the narrow ring and the stepped ring cavity the shoe velocity was varied in further simulations. The resulting densities after one shoe passage using three different velocities are displayed in Fig. 11. In the case of the narrow ring the density distributions are more inhomogeneous for low shoe velocities. The strongest surface densification and the most pronounced density dependency on the azimuthal angle is observed for the lowest velocity. In the stepped ring the distributions are very similar for all three velocities. Thus, lowering the shoe velocity does not generally help to improve homogeneity.

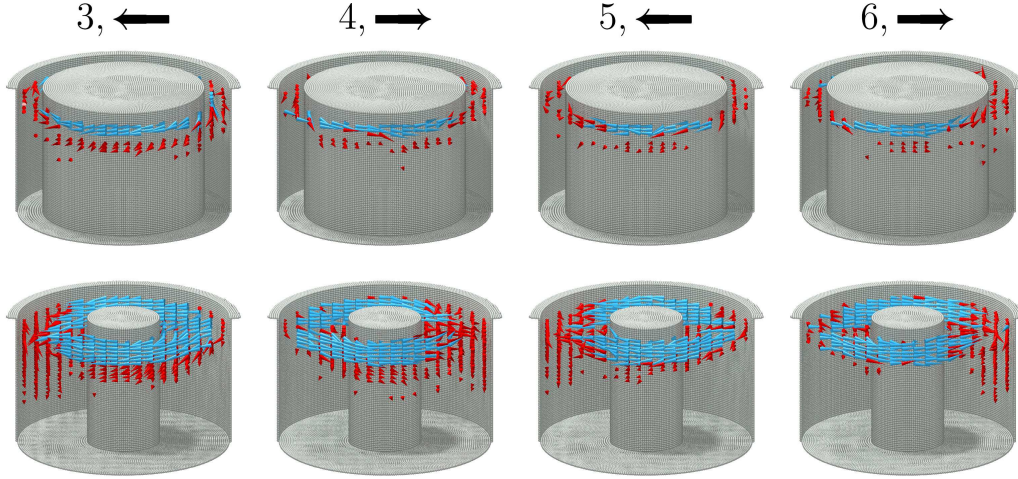


Fig. 10. Grain displacements between subsequent shoe passages, labeled by passage number and direction. Each arrow head points towards the direction of the average grain displacement at its position. The length of the red (dark) arrows is proportional to the displacement magnitude. Blue (light) arrows represent displacements above a threshold of 0.5 mm and have constant length. For better visibility all arrows are scaled up by a factor of five. Displacements below 0.1 mm and displacements of grains newly entering the cavities are not drawn.

4.5 Cavity and shoe vibrations

The effect of sinusoidal oscillations of the shoe or the cavity during or after the filling stage was investigated for the narrow ring cavity. The shoe velocity was 0.09 m/s in all cases.

First, oscillations with a frequency $f=32$ Hz and an amplitude of 1 mm in the direction of the feeding shoe motion (x -axis) were applied during the filling stage. The oscillation frequency f is the inverse of the oscillatory period. Figure 12 shows the density distribution after the passage of the feeding shoe. Shaking the shoe does not alter the density significantly compared to the case without any oscillations (see bottom left panel of Fig 11). However, cavity

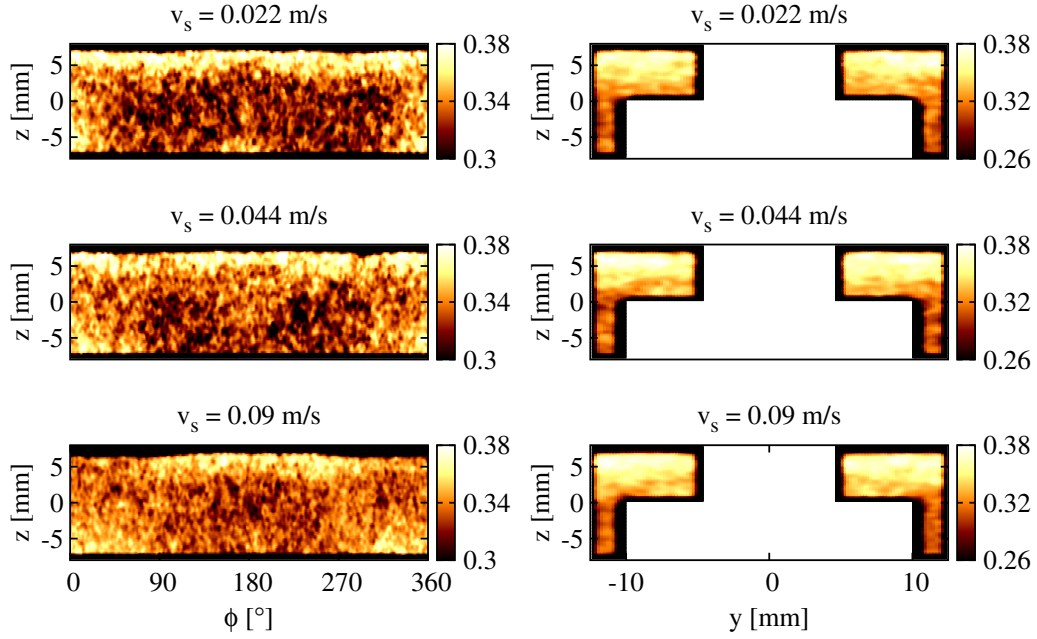


Fig. 11. Density distributions using varied shoe velocities for the narrow ring and the stepped ring.

oscillations have a strong impact on the distribution. The average density increases and angular density variations appear. The cavity sections oriented parallel to the axis of oscillation (i.e. $90^\circ/270^\circ$ for shaking along the x -axis) are denser than those perpendicular to it.

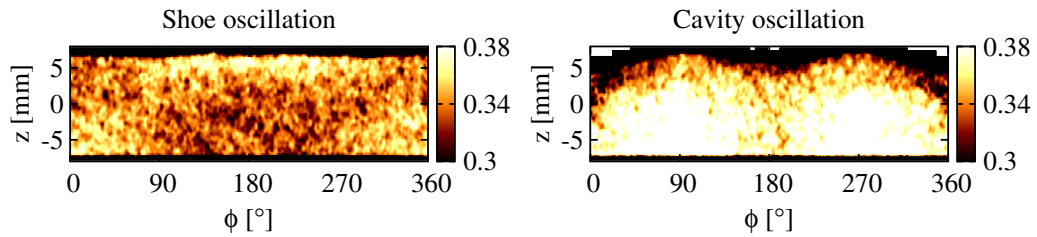


Fig. 12. Densities for the narrow ring cavity under oscillations along the x -axis during the filling stage.

Second, cavity oscillations with 1 mm amplitude perpendicular to the shoe motion (i.e. in the y -direction) were applied after the shoe passage. The fre-

quency was varied between 2 Hz and 32 Hz. Figure 13 shows the results. Up to 8 Hz the density distribution remains unaffected compared to the case without any oscillations. At 20 Hz strong densification near the $0^\circ/360^\circ$ and 180° positions occur reaching from the surface downwards into the cavity. At 32 Hz the situation is reversed and densification is pronounced in the lower half of the cavity. Note, that the density distribution for $f=32$ Hz is very similar to the case of cavity oscillation during filling (Fig. 12) except for the different shaking direction. Thus, it appears to be unimportant whether the oscillations are applied during or after the filling stage.

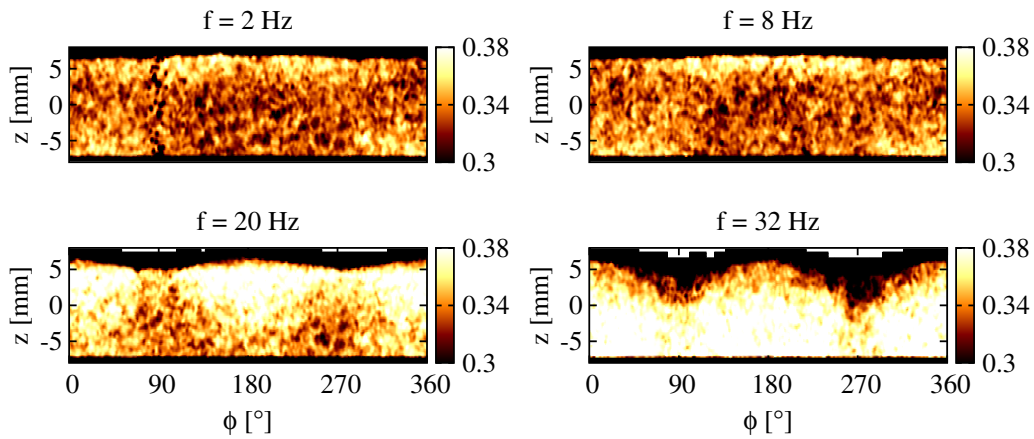


Fig. 13. Densities for the narrow ring cavity under varied oscillation frequencies along the y -axis after the filling stage.

In order to overcome the anisotropy caused by linear oscillations, the influence of rotational oscillations was investigated. The motion of each point of the cavity is described by

$$\mathbf{r}(t) = \begin{pmatrix} \cos(\theta(t)) & -\sin(\theta(t)) & 0 \\ \sin(\theta(t)) & \cos(\theta(t)) & 0 \\ 0 & 0 & 1 \end{pmatrix} \mathbf{r}(0), \quad \theta(t) = \theta_0 \sin(2\pi ft), \quad (14)$$

where the origin of the coordinate system lies in the center of the cavity. Thus, the axis of rotation is the z -axis. The rotational oscillation amplitude θ_0 was varied between 1.25° and 80° . $\theta_0=5^\circ$ correspond to a displacement of 1 mm at the circumference of the ring. The frequency f was varied between 2 Hz and 32 Hz.

Figure 14 shows density maps using rotational oscillations applied for $t_{\text{rot}}=0.7$ s after filling with $v_s=0.09$ m/s. For 5° and 2 Hz or 1.25° and 8 Hz, respectively, the effect of the oscillations is negligible. However, using 5° and 8 Hz the density distribution becomes significantly more homogeneous. For 20° and 8 Hz or 5° and 32 Hz angular density gradients vanish completely, the overall density increases and the filling height decreases as a direct consequence. For 80° and 8 Hz the density distribution is slightly less homogeneous due to regions of higher density at the bottom of the cavity. In summary, the effect of increasing f while keeping θ_0 constant (left panel of Fig. 14) is similar to the effect of increasing θ_0 with constant f (right panel of Fig. 14).

The influence of the duration of the applied oscillations, t_{rot} , was tested for the case of $\theta_0=5^\circ$ and $f=32$ Hz. The results are displayed in Fig. 15 in addition to the lower left panel of Fig. 14 ($t_{\text{rot}}=0.7$ s). The density increases and the distribution becomes more homogeneous over time. Thus, for the present cavity it is beneficial to apply rotational oscillations for about 1 s. The effect of longer oscillation durations was not studied.

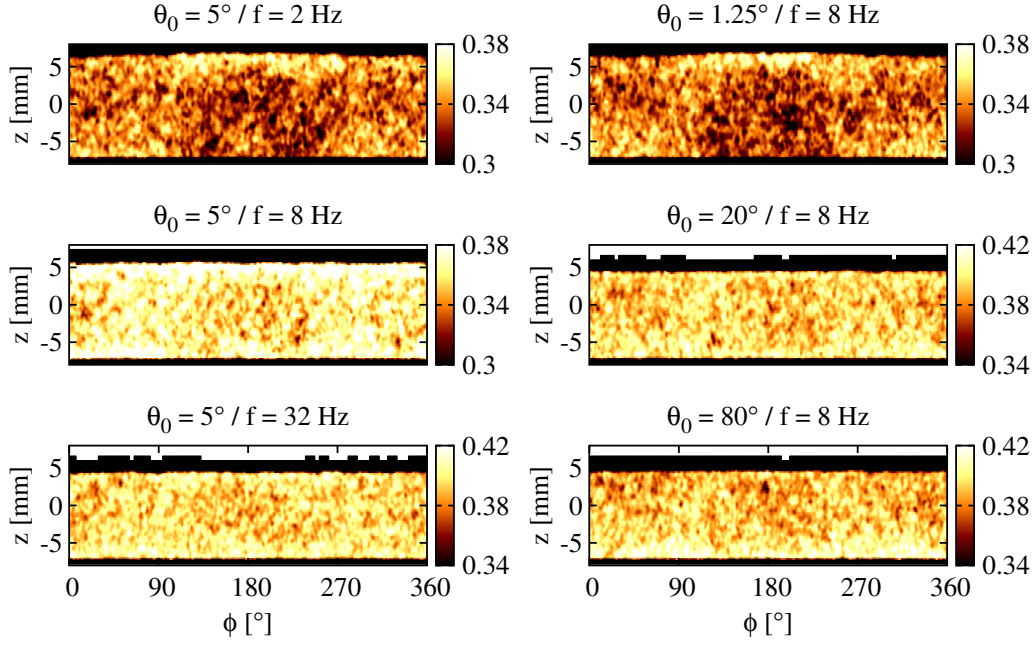


Fig. 14. Densities for the narrow ring cavity using different rotational oscillation amplitudes and frequencies.

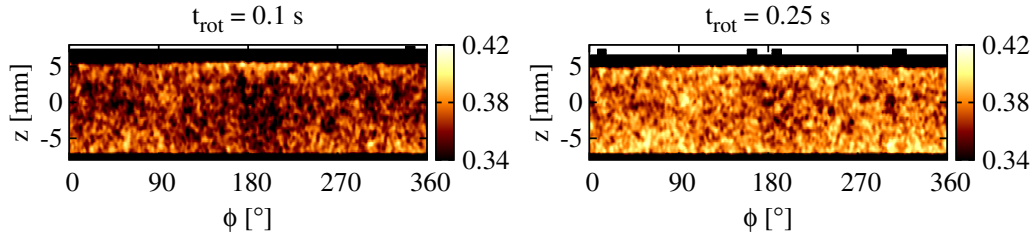


Fig. 15. Densities for the narrow ring cavity using varied durations of rotational oscillations.

4.6 Volumetric filling

The technical term *volumetric filling* means that the lower punches of the tool set suck the powder into the die cavity from the feeding shoe, which may stop or move during this operation (see Fig. 16 for details). Figure 17 displays density distributions using volumetric filling with varied punch velocities, v_{punch} .

Shoe oscillations were applied during the punch movement, because arching occurred in the narrow ring without oscillations and the powder would not fall into the cavity. The shoe starts to move again with $v_s=0.09$ m/s when the punches have reached their final position.

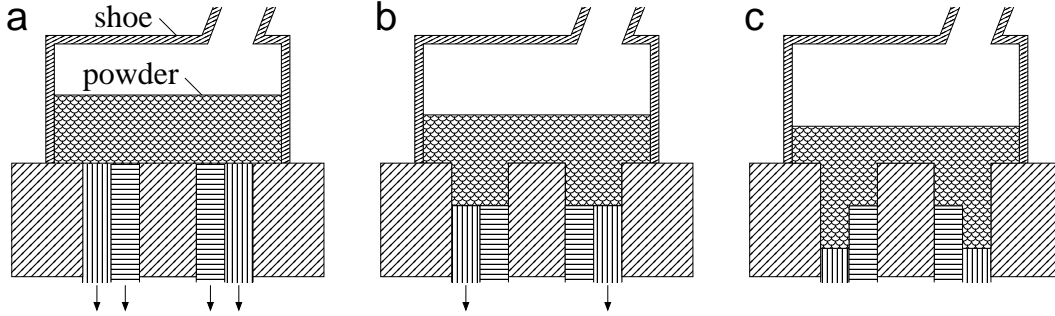


Fig. 16. Schematic of the volumetric filling process as applied in this work. The punches start to move after the shoe stops.

For the narrow ring volumetric filling with $v_{\text{punch}}=0.01$ m/s yields a homogeneous distribution without azimuthal density gradients. For $v_{\text{punch}}=0.02$ m/s the density is slightly higher at the bottom of the cavity compared to half height. The cavity is not filled completely for higher punch velocities, because the grains fall slower than the punch moves and the shoe starts moving again too early. However, this effect can partly be understood as an artifact due to the lack of explicit air modeling. In the present model the moving punches do not actively suck the powder into the cavity. The punches rather make room for the powder to fall freely.

For the stepped ring cavity the results do not depend on the punch velocity. The density in the lower narrow part is increased in comparison to the case of conventional filling (see right panel of Fig. 11) and comparable to the density in the upper wide part. However, a region of lower density exists at the transition between the wide and narrow part.

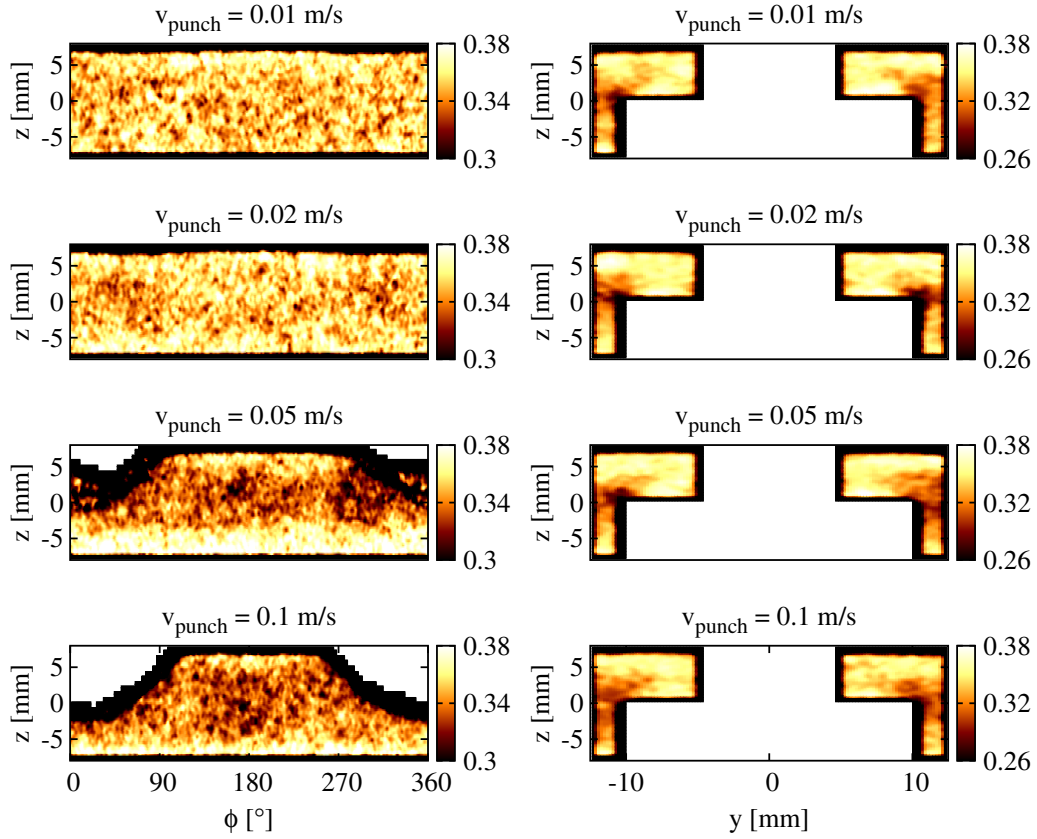


Fig. 17. Densities for the narrow and stepped ring cavity using volumetric filling. The filling is supported by shoe oscillations.

4.7 Density homogeneity index

In this section an index for the quantitative description of the homogeneity of a density distribution is defined and calculated for three setups from the present study. The index is based on the probability density function (PDF) of the spatial density distribution. The PDF is obtained numerically by creating a histogram from the underlying data. Figure 18 displays density PDFs for three exemplary filling methods using the narrow ring cavity: First, conventional filling with $v_s=0.09$ m/s (see Fig. 11). Second, volumetric filling using $v_{\text{punch}}=0.02$ m/s (see Fig. 17). Third, filling with subsequent rotational cav-

ity oscillations using $\theta_0=5^\circ$ and $f=32$ Hz (see Fig. 14). The nonvanishing low probabilities besides the main peaks correspond to the boundary zones at the cavity walls.

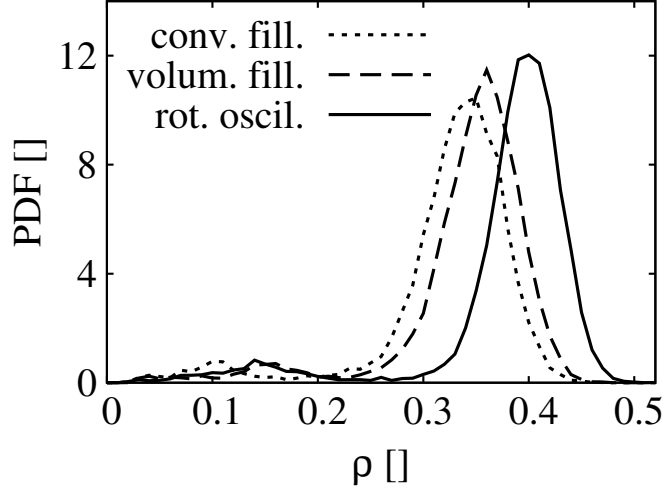


Fig. 18. PDFs of the density ρ obtained from different die filling methods.

The density homogeneity index (DHI) is calculated as follows. First, the PDF is restricted to its main peak in order to consider only the bulk density. Therefore, a threshold, ρ_{thr} , is defined in relation to the density value with the highest probability, ρ_{peak} :

$$\rho_{\text{thr}} = 0.6 \rho_{\text{peak}}. \quad (15)$$

The value of 0.6 is chosen arbitrarily but proved to be adequate for the present data. The part of the PDF with $\rho \geq \rho_{\text{thr}}$ is referred to as restricted PDF. The DHI is obtained as the scaled quotient of the standard deviation, ρ_σ , and the expected value, ρ_{exp} , of the restricted PDF:

$$\text{DHI} = 100 \frac{\rho_\sigma}{\rho_{\text{exp}}}. \quad (16)$$

Clearly, a lower DHI indicates a more homogeneous distribution.

Table 2 gives a summary of the DHIs and related quantities for the evaluated

Table 2

Density homogeneity indices and statistical quantities of the (restricted) PDFs as shown in Fig. 18.

Method	ρ_{peak}	ρ_{thr}	ρ_{exp}	ρ_{σ}	DHI
conventional filling	0.35	0.21	0.338	0.00373	11.0
volumetric filling	0.36	0.22	0.354	0.00361	10.2
rotational oscillations	0.40	0.24	0.396	0.00326	8.2

filling methods. A comparison of the DHIs confirms that the homogeneity of the density distribution is improved by using volumetric filling or applying rotational oscillations.

5 Discussion

It was demonstrated that observed features of density distributions after filling can be reproduced and, thus, predicted by DEM simulations. A simple way of model parameter adjustment was used to match the filling behavior observed in the experiment using the irregular shaped Distaloy AE powder.

Two types of model grains were used in the simulations. On the one hand, rigidly connected primary spheres form grains containing a certain geometrical complexity. On the other hand, simple spheres without rotational degrees of freedom were employed as grain representations. Both models proved to perform similarly well in predicting density features. A typical filling simulation takes about 4500 CPU hours on a Xeon 2.0 GHz system using the multi-sphere model. The computing time is reduced by a factor of ten if the single sphere

model with comparable grain size is used. However, the multi-sphere model should be preferred for DEM studies focusing on the relation between physically sound grain interaction and macroscopic flow behavior [14].

Simulations with up to ten times larger grain diameters than in reality are able to predict significant density features. The simulations only fail when grain diameters are comparable to cavity dimensions.

The density distribution appears to be strongly determined by the cavity geometry. In the case of incomplete filling the feeding shoe velocity does also affect the density significantly. The shoe velocity has less influence if the cavity is filled completely after one shoe passage.

After grains have settled in the cavity they stay at their positions and the local density remains constant. The kinetic energy of newly arriving grains does only contribute to slight densification of the current surface.

Regarding subsequent shoe passages two propositions of the compaction model of Hjortsberg *et al.* [31] could be verified by the present simulations: Grain rearrangement and, thus, densification is limited to a certain depth and it is less pronounced at the location where the shoe meets the cavity first. In addition, it was shown that the compaction depth is correlated with grain size. Therefore, it is necessary to simulate the process with realistic grain sizes if the effect of surface densification is not to be overestimated.

Cavity oscillations affect the density strongly and can be used to homogenize the distribution. However, oscillations might as well introduce inhomogeneities, if they do not respect the symmetry of the cavity. Thus, rotational oscillations turn out to be helpful for a ring cavity [33]. The effect of increasing

the amplitude or the frequency of the oscillations is comparable. It is evident that the application of cavity oscillations might not be easily implemented in a given die compaction system. However, by using simulations the possible improvements of these technique can be estimated.

Volumetric filling by punch movement proved to be helpful for homogenization, because intrinsic anisotropies caused by the direction of shoe movement are avoided. However, the build up of arches must be avoided in slender cavities e.g. by some shaking.

6 Conclusion

Coarse grained DEM models were introduced for simulating the die filling process in three dimensions. Comparisons of measured and calculated density distributions for different cavities showed good qualitative and partially even quantitative agreement. Thus, DEM simulations render the prediction of density distributions in realistic cavity geometries possible if an appropriate 3D simulation code and thoroughly determined model parameters are used.

Density inhomogeneities are mainly influenced by the combination of cavity geometry and feeding shoe velocity. A schematic model for redensification in subsequent shoe passages proposed by Hjortsberg *et al.* [31] could be confirmed. Cavity oscillations during or after the filling stage strongly affect the density distribution throughout the die. This effect can be utilized for homogenization. Another approach to achieve more homogeneous density distributions is given by volumetric filling.

A density homogeneity index, DHI, was introduced based on the PDF of the

density distribution. The DHI provides a convenient scalar measure for the homogeneity of the distribution.

Further DEM studies on die filling should assess the influence of particle size distributions on the density. Size segregation might occur during filling or as a result of oscillations. The influence of air on powder flow is significant in deep and narrow cavities, especially when small and light grains are used [34,35,9,10]. An efficient method for coupling the DEM computations with a solver for air flow in 3D is therefore desirable. Yet, already the present models reveal detailed insight in the formation of density distributions and prove to be a helpful tool for optimization of the filling process.

Acknowledgments

We gratefully acknowledge financial support from the Landesstiftung Baden-Württemberg and the Fraunhofer project *CerGran-Füllen*. Calculations were performed on the computer clusters at Fraunhofer EMI, ITWM, and IWM.

References

- [1] R. M. German. *Sintering Theory and Practice*. Wiley-VCH, 1996.
- [2] C. Y. Wu and A. C. F. Cocks. Flow behaviour of powders during die filling. *Powder Metall.*, 47(2):127–136, 2004.
- [3] W. Schatt and K.-P. Wieters. *Powder Metallurgy: Processing and Materials*. EPMA, 1997.
- [4] S. F. Burch, A. C. F. Cocks, J. M. Prado, and J. H. Tweed. *Modelling of Powder Die Compaction*, chapter 9 – Die Fill and Powder Transfer. Springer, 2007.
- [5] D. Korachkin, D. T. Gethin, R. W. Lewis, and J. H. Tweed. Effect of Die Filling on Powder Compaction. *Int. J. Powder Metall.*, 44(1):22–34, 2008.
- [6] O. Coube, A. C. F. Cocks, and C. Y. Wu. Experimental and numerical study of die filling, powder transfer and die compaction. *Powder Metall.*, 48(1):68–76, 2005.
- [7] C. Y. Wu, A. C. F. Cocks, and O. T. Gillia. Die filling and powder transfer. *Int. J. Powder Metall.*, 39(4):51–64, 2003.
- [8] C. Y. Wu and A. C. F. Cocks. Numerical and experimental investigations of the flow of powder into a confined space. *Mech. Mater.*, 38(4):304–324, 2006.
- [9] Y. Guo, K. D. Kafui, C. Thornton, and C. Y. Wu. A Numerical Study of Die Filling Using a Coupled Discrete Element Method and Computational Fluid Dynamics. In *Proceedings of the EURO PM2007, Volume 3, Toulouse, France*, pages 317–322, Shrewsbury, UK, 2007. EPMA.
- [10] Y. Guo, K. D. Kafui, C. Y. Wu, C. Thornton, and J. P. K. Seville. A coupled DEM/CFD analysis of the effect of air on powder flow during die filling. *AICHE J.*, 55(1):49–62, 2009.

- [11] P. A. Cundall and O. D. L. Strack. A discrete numerical model for granular assemblies. *Geotechnique*, 29(1):47–65, 1979.
- [12] M. D. Riera, A. Istúriz, J. M. Prado, J. C. Cante, J. Oliver, and C. González. Experimental and Numerical Study of the Die Filling Stage in Powder Metallurgy. In *Proceedings of the EURO PM2005, Volume 3, Prague, Czech Republic*, pages 339–344, Shrewsbury, UK, 2005. EPMA.
- [13] G. Gustafsson and H.-Å. Häggblad. Simulation of Metal Powder Die Filling Processes Using Smoothed Particle Hydrodynamics Method. In *Proceedings of the EURO PM2007, Volume 3, Toulouse, France*, pages 311–316, Shrewsbury, UK, 2007. EPMA.
- [14] C. Bierwisch, T. Kraft, H. Riedel, and M. Moseler. Three-dimensional discrete element models for the granular statics and dynamics of powders in cavity filling. *J. Mech. Phys. Solids*, 57(1):10–31, 2009.
- [15] C. S. Campbell and C. E. Brennen. Computer simulation of granular shear flows. *J. Fluid Mech.*, 151:167–188, 1985.
- [16] O. R. Walton and R. L. Braun. Stress calculations for assemblies of inelastic spheres in uniform shear. *Acta Mech.*, 63(1):73–86, 1986.
- [17] P. K. Haff and B. T. Werner. Computer simulation of the mechanical sorting of grains. *Powder Technol.*, 48(3):239–245, 1986.
- [18] J. A. C. Gallas, H. J. Herrmann, and S. Sokołowski. Convection cells in vibrating granular media. *Phys. Rev. Lett.*, 69(9):1371–1374, 1992.
- [19] R. García-Rojo, H. J. Herrmann, and S. McNamara, editors. *Powders and Grains 2005*, Leiden, 2005. Balkema.
- [20] M. P. Allen and D. J. Tildesley. *Computer Simulation of Liquids*. Oxford University Press, 1987.

- [21] C. Y. Wu. DEM simulations of die filling during pharmaceutical tableting. *Particuology*, 6(6):412–418, 2008.
- [22] T. Pöschel and V. Buchholtz. Static Friction Phenomena in Granular Materials: Coulomb Law versus Particle Geometry. *Phys. Rev. Lett.*, 71(24):3963–3966, 1993.
- [23] I. P. Omelyan. On the numerical integration of motion for rigid polyatomics: The modified quaternion approach. *Comput. Phys.*, 12(1):97–103, 1998.
- [24] H. Hertz. Über die Berührung fester elastischer Körper. *Journal für die reine und angewandte Mathematik, Leipzig*, 92:156–171, 1881.
- [25] K. L. Johnson, K. Kendall, and A. D. Roberts. Surface energy and the contact of elastic solids. *Proc. R. Soc. London, Ser. A*, 324(1558):301–313, 1971.
- [26] E. D. Landau and E. M. Lifshitz. *Theory of Elasticity*. Pergamon Press, 1970.
- [27] L. E. Silbert, D. Ertas, G. S. Grest, T. C. Halsey, D. Levine, and S. J. Plimpton. Granular flow down an inclined plane: Bagnold scaling and rheology. *Phys. Rev. E*, 64(5):051302, 2001.
- [28] L. E. Silbert, D. Ertas, G. S. Grest, T. C. Halsey, and D. Levine. Geometry of frictionless and frictional sphere packings. *Phys. Rev. E*, 65(3):031304, 2002.
- [29] G. H. Ristow. Outflow rate and wall stress for two-dimensional hoppers. *Physica A*, 235(3):319–326, 1997.
- [30] D. Korachkin, D. T. Gethin, and J. H. Tweed. Friction Measurement Using a Die Shear Plate Equipment. In *Proceedings of the EURO PM2005, Volume 3, Prague, Czech Republic*, pages 369–375, Shrewsbury, UK, 2005. EPMA.
- [31] E. Hjortsberg and B. Bergquist. Filling induced density variations in metal powder. *Powder Metall.*, 45(2):146–153, 2002.

- [32] G. F. Bocchini. Influence of small die width on filling and compacting densities. *Powder Metall.*, 30(4):261–266, 1987.
- [33] C. Bierwisch, T. Kraft, H. Riedel, and M. Moseler. Verfahren zur Homogenisierung einer Pulverschüttung bei der Herstellung von Pulverpresslingen, pending patent application.
- [34] C. Y. Wu, L. Dihoru, and A. C. F. Cocks. The flow of powder into simple and stepped dies. *Powder Technol.*, 134(1-2):24–39, 2003.
- [35] L. C. R. Schneider, A. C. F. Cocks, and A. Apostolopoulos. Comparison of filling behaviour of metallic, ceramic, hardmetal and magnetic powders. *Powder Metall.*, 48(1):77–84, 2005.